

# Next-to-Leading Order Analysis of Target Mass Corrections to Structure Functions and Asymmetries

L. T. Brady<sup>1,2</sup>, A. Accardi<sup>1,3</sup>, T. J. Hobbs<sup>1,4</sup>, W. Melnitchouk<sup>1</sup>

<sup>1</sup>*Jefferson Lab, Newport News, Virginia 23606*

<sup>2</sup>*Harvey Mudd College, Claremont, California 91711*

<sup>3</sup>*Hampton University, Hampton, Virginia 23668*

<sup>4</sup>*Indiana University, Bloomington, Indiana 47405*

## Abstract

We perform a comprehensive analysis of target mass corrections (TMCs) to spin-averaged structure functions and asymmetries at next-to-leading order. Several different prescriptions for TMCs are considered, including the operator product expansion, and various approximations to it, collinear factorization, and  $\xi$ -scaling. We assess the impact of each of these on a number of observables, such as the neutron to proton  $F_2$  structure function ratio, and parity-violating electron scattering asymmetries for protons and deuterons which are sensitive to  $\gamma Z$  interference effects. The corrections from higher order radiative and nuclear effects on the parity-violating deuteron asymmetry are also quantified.

## I. INTRODUCTION

Tremendous progress has been made in recent years in the quest to reveal the structure of the nucleon at its deepest levels. Traditionally deep-inelastic scattering (DIS) of leptons has been the primary tool used to study nucleon structure at large values of the four-momentum transfer squared,  $Q^2$ , where the nucleon's quark and gluon (or parton) constituents can be cleanly resolved. Here the theoretical tools are well developed, and the nucleon's structure can be conveniently parametrized in terms of universal longitudinal momentum distribution functions of individual quarks and gluons. Global analyses of DIS and other hard processes have been highly successful in correlating data over a wide range of kinematics, producing fits of parton distribution functions (PDFs) to next-to-leading order (in the strong coupling parameter  $\alpha_s$ ) accuracy and beyond [1–8].

While the perturbative domain of large  $Q^2$  and small parton momentum fraction  $x$  has received considerable attention both experimentally and theoretically, the region of large  $x$  and low  $Q^2$  ( $\sim 1 - 2 \text{ GeV}^2$ ), where nonperturbative effects play a greater role, has been relatively poorly explored. This is perhaps not too surprising given the difficulty in reliably computing the various corrections that are needed to describe data in this region. Examples of nonperturbative effects that are relevant here include target mass corrections (TMCs) associated with finite values of  $M^2/Q^2$ , where  $M$  is the nucleon mass, higher twist terms arising from long-range nonperturbative multi-parton correlations, and nuclear corrections in experiments involving deuterium or heavier nuclei, which are important at large  $x$  for any  $Q^2$ .

The large- $x$  region has been particularly difficult to access experimentally, especially in high-energy colliders, due to the rapidly falling cross sections as  $x \rightarrow 1$ . The most extensive data set available that covers this region has been from experiments at SLAC [9]. More recently, progress on this front has been made with DIS structure function measurements at Jefferson Lab, utilizing the high luminosities and duty factors available with the CEBAF accelerator. Indeed, an impressive body of very high-precision data has now been accumulated over the last decade on various structure functions, including accurate longitudinal–transverse separations needed for model-independent determinations of the  $F_2$  and  $F_L$  structure functions of protons and nuclei [10]. Future plans at the energy upgraded Jefferson Lab involve extending the DIS measurements to even larger  $x$  ( $x \sim 0.85$ ) with

planned experiments [11–13] to measure the ratio of  $d$  to  $u$  quark distributions, as well as search for effects such as charge symmetry violation in PDFs and tests of the Standard Model in parity-violating DIS asymmetries.

The new data have the potential to provide strong constraints on PDFs at large  $x$ , where currently uncertainties remain significant. Several recent analyses [6, 7] have in fact attempted to utilize data at low values of  $Q^2$  and invariant final state hadron masses  $W^2 = M^2 + Q^2(1 - x)/x$ . Stable fits of leading twist PDFs could be obtained [6] for  $W$  down to  $\sim 3$  GeV and  $Q^2 \gtrsim 1.7$  GeV<sup>2</sup>, as long as TMC and higher twist corrections were accounted for. Aside from its intrinsic value, better knowledge of PDFs at large  $x$  may also be important for searches of new physics signals in collider experiments such as at the Tevatron or the LHC at large rapidities or for heavy mass particles [14], as well as at more central rapidities where uncertainties in large- $x$  PDFs at low  $Q^2$  can, through  $Q^2$  evolution, affect cross sections at small  $x$  and large  $Q^2$  [15].

The increased kinematic reach of the future high-precision DIS measurements calls for a careful evaluation of the relevant nonperturbative corrections in order to unambiguously extract information on leading twist PDFs or new physics signals. The effects that are most amenable to direct computation, in principle, are the TMCs. As discussed by Nachtmann [16], these effects are in fact associated with leading twist operators (hence contain no additional information on the nonperturbative parton correlations), even though they give rise to  $Q^2/\nu^2 = 4x^2M^2/Q^2$  corrections, where  $\nu = Q^2/2Mx$  is the energy transfer. Nachtmann further showed that one could generalize the standard operator product expansion (OPE) of structure function moments to finite  $Q^2$  such that only operators of a specific twist would appear at a given order in  $1/Q^2$ . The resulting target mass corrected structure functions can then be derived through an inverse Mellin transformation, as shown by Georgi and Politzer [17] (for a review of TMCs in the OPE approach see Ref. [18]).

Later an alternative formulation in terms of collinear factorization (CF) was used by Ellis, Furmanski and Petronzio [19] to derive TMCs including the effects of off-shell partons and parton transverse motion. While the OPE and CF formulations yield identical results for leading twist PDFs, they differ in the details of how the target mass corrections are manifested at finite  $Q^2$ . Other versions of TMCs were subsequently derived [20–22] within the CF formalism using various assumptions about the intrinsic properties of partons and higher twist contributions, leading to rather large differences in some cases [22]. Some

of the phenomenological implications of the different TMC prescriptions were discussed in Refs. [21, 22], including differences between leading order and next-to-leading order (NLO) results; however, the effects on observables have not been systematically investigated. We do so in this paper.

In Sec. II we summarize the main results for TMCs in the OPE and various CF formulations for the  $F_1$ ,  $F_2$ ,  $F_3$  and  $F_L$  structure functions at NLO, and illustrate the differences numerically. Implications for various observables are discussed in Sec. III, including the ratio of neutron to proton  $F_2$  structure functions, which constrain the  $d/u$  PDF ratio at large  $x$ , longitudinal to transverse cross section ratios  $R$ , and parity-violating (PV) DIS asymmetries on the proton and deuteron which are sensitive to  $\gamma Z$  interference structure functions. We also quantify the effects of perturbative NLO corrections on the  $R^{\gamma Z}$  ratio for the  $\gamma Z$  interference, about which nothing is known empirically, and of nuclear effects on the deuteron PV asymmetries. Some finite- $Q^2$  effects on PV asymmetries were investigated previously in Ref. [23, 24], and higher-twists in deuteron PV asymmetries in Refs. [25–29]. Finally, in Sec. IV we draw some conclusions and outline possible extensions of this work.

## II. TARGET MASS CORRECTIONS

In this section we review the kinematic corrections to structure functions arising from scattering at finite values of  $Q^2/\nu^2$ . We consider several frameworks for the TMCs, including the conventional one based on the operator product expansion, and various approximations to it, as well as a number of prescriptions using collinear factorization at leading and next-to-leading order in  $\alpha_s$ . The structure functions for the scattering of an unpolarized lepton from an unpolarized nucleon are defined in terms of the nucleon hadron tensor [30],

$$W_{\mu\nu} = \frac{1}{4\pi} \int d^4z e^{iq \cdot z} \langle p | [J_\mu^\dagger(z), J_\nu(0)] | p \rangle \quad (1a)$$

$$= \left( -g_{\mu\nu} + \frac{q_\mu q_\nu}{q^2} \right) F_1(x, Q^2) + \left( p_\mu - \frac{p \cdot q}{q^2} q_\mu \right) \left( p_\nu - \frac{p \cdot q}{q^2} q_\nu \right) \frac{F_2(x, Q^2)}{p \cdot q} - i\epsilon_{\mu\nu\alpha\beta} q^\alpha p^\beta \frac{F_3(x, Q^2)}{2p \cdot q}, \quad (1b)$$

where  $J_\mu$  is the electromagnetic or weak current operator for a given virtual boson ( $\gamma$ ,  $Z$  or  $W^\pm$ ). Here  $p$  and  $q$  are the nucleon and exchanged boson four-momenta, respectively, with  $q^2 = -Q^2$ .

The structure functions  $F_{1,2}$  are related to the product of two vector or two axial-vector currents, while  $F_3$  arises from the interference of vector and axial-vector currents. The  $F_1$  structure function is proportional to the transverse virtual boson cross section, and  $F_2$  is given by a combination of transverse and longitudinal cross sections. It is convenient to also introduce the longitudinal structure function,

$$F_L(x, Q^2) = \rho^2 F_2(x, Q^2) - 2xF_1(x, Q^2), \quad (2)$$

where

$$\rho^2 = 1 + \frac{4x^2 M^2}{Q^2}. \quad (3)$$

In the following we will summarize target mass corrections for each of these structure functions computed within the various approaches outlined above.

### A. Operator product expansion

Target mass corrections to structure functions were first systematically considered by Georgi and Politzer [17] in the framework of the operator product expansion. Here the twist-two quark bilinears in the product of currents  $J_\mu J_\nu$  in Eq. (1a) are modified with the introduction of covariant derivatives,  $\bar{\psi}\gamma^\mu D^{\mu_1} \dots D^{\mu_n} \psi$ ; since each derivative  $D^{\mu_i}$  increases both the dimension and spin of the operator by one unit, the twist (dimension minus spin) remains unchanged. The expansion in terms of covariant derivatives yields a series in  $1/Q^2$  with coefficients given by moments of structure functions. The resulting target mass corrected structure functions are then accessed through an inverse Mellin transformation, which gives [17]

$$F_1^{\text{OPE}}(x, Q^2) = \frac{1+\rho}{2\rho} F_1^{(0)}(\xi, Q^2) + \frac{\rho^2-1}{4\rho^2} \left[ h_2(\xi, Q^2) + \frac{\rho^2-1}{2x\rho} g_2(\xi, Q^2) \right], \quad (4a)$$

$$F_2^{\text{OPE}}(x, Q^2) = \frac{(1+\rho)^2}{4\rho^3} F_2^{(0)}(\xi, Q^2) + \frac{3x(\rho^2-1)}{2\rho^4} \left[ h_2(\xi, Q^2) + \frac{\rho^2-1}{2x\rho} g_2(\xi, Q^2) \right], \quad (4b)$$

$$F_L^{\text{OPE}}(x, Q^2) = \frac{(1+\rho)^2}{4\rho} F_L^{(0)}(\xi, Q^2) + \frac{x(\rho^2-1)}{\rho^2} \left[ h_2(\xi, Q^2) + \frac{\rho^2-1}{2x\rho} g_2(\xi, Q^2) \right], \quad (4c)$$

$$F_3^{\text{OPE}}(x, Q^2) = \frac{(1+\rho)}{2\rho^2} F_3^{(0)}(\xi, Q^2) + \frac{(\rho^2-1)}{2\rho^3} h_3(\xi, Q^2), \quad (4d)$$

where  $F_i^{(0)}$  are the structure functions in the  $M^2/Q^2 \rightarrow 0$  limit, evaluated at the modified scaling variable  $\xi$  [16, 31],

$$\xi = \frac{2x}{1+\rho}, \quad (5)$$

which approaches  $x$  as  $M^2/Q^2 \rightarrow 0$ . The functions  $h_2$ ,  $g_2$  and  $h_3$  are associated with higher order terms in  $M^2/Q^2$  and are given by [17, 18]

$$h_2(\xi, Q^2) = \int_{\xi}^1 du \frac{F_2^{(0)}(u, Q^2)}{u^2}, \quad (6a)$$

$$g_2(\xi, Q^2) = \int_{\xi}^1 du \int_u^1 dv \frac{F_2^{(0)}(v, Q^2)}{v^2} = \int_{\xi}^1 du (u - \xi) \frac{F_2^{(0)}(u, Q^2)}{u^2}, \quad (6b)$$

$$h_3(\xi, Q^2) = \int_{\xi}^1 du \frac{F_3^{(0)}(u, Q^2)}{u}. \quad (6c)$$

(Note that the function  $g_2$  here should not be confused with the spin-dependent  $g_2$  structure function measured in polarized lepton–nucleon scattering.)

The expressions in Eqs. (4) are known to suffer from the “threshold problem”, in which the target mass corrected (leading twist) structure functions do not vanish as  $x \rightarrow 1$ , and are in fact nonzero in the kinematically forbidden  $x > 1$  region, where for a proton target baryon number conservation would be violated. This is clear from the  $\mathcal{O}(1)$  terms in Eqs. (4) in which the massless functions  $F_i^{(0)}$  are evaluated at  $\xi$ . Because at any finite  $Q^2$  value one has  $\xi < \xi_0 \equiv \xi(x = 1) < 1$ , for any input function  $F_i^{(0)}$  which is nonzero for  $0 < x < 1$ , the target mass corrected function at  $x = 1$  will not vanish,  $F_i^{\text{OPE}}(x = 1, Q^2 < \infty) > 0$ . A number of attempts have been made to ameliorate the threshold problem [32, 33] using various prescriptions and *ansätze*, although none of these is unique and without additional complications [18].

Recently, Kulagin and Petti [34] showed that by expanding the target mass corrected structure functions to leading order in  $1/Q^2$ , the resulting functions have the correct  $x \rightarrow 1$  limits,

$$F_1^{1/Q^2}(x, Q^2) = \frac{1}{4} (5 - \rho^2) F_1^{(0)}(x, Q^2) - \frac{1}{4} (\rho^2 - 1) \left[ x F_1^{(0)'}(x, Q^2) - h_2(x, Q^2) \right], \quad (7a)$$

$$F_2^{1/Q^2}(x, Q^2) = (2 - \rho^2) F_2^{(0)}(x, Q^2) - \frac{1}{4} (\rho^2 - 1) \left[ x F_2^{(0)'}(x, Q^2) - 6x h_2(x, Q^2) \right], \quad (7b)$$

$$F_L^{1/Q^2}(x, Q^2) = F_L^{(0)}(x, Q^2) - \frac{1}{4} (\rho^2 - 1) \left[ x F_L^{(0)'}(x, Q^2) - 4x h_2(x, Q^2) \right], \quad (7c)$$

$$F_3^{1/Q^2}(x, Q^2) = \frac{1}{4} (7 - 3\rho^2) F_3^{(0)}(x, Q^2) - \frac{1}{4} (\rho^2 - 1) \left[ x F_3^{(0)'}(x, Q^2) - 2h_3(x, Q^2) \right]. \quad (7d)$$

While avoiding the threshold problem, this prescription, however, raises the question of whether the  $1/Q^2$  approximation is sufficiently accurate for structure functions near  $x \approx 1$

at moderate  $Q^2$ . To test the convergence of the  $1/Q^2$  expansion at large  $x$ , we further expand the OPE results (4) to include  $\mathcal{O}(1/Q^4)$  corrections,

$$F_1^{1/Q^4}(x, Q^2) = F_1^{1/Q^2}(x, Q^2) + (\rho^2 - 1)^2 \left[ \frac{3}{16} F_1^{(0)}(x, Q^2) + \frac{1}{16x} F_2^{(0)}(x, Q^2) \right. \\ \left. + \frac{3x}{16} F_1^{(0)'}(x, Q^2) + \frac{x^2}{32} F_1^{(0)''}(x, Q^2) - \frac{1}{4} h_2(x, Q^2) + \frac{1}{8x} g_2(x, Q^2) \right] \quad (8a)$$

$$F_2^{1/Q^4}(x, Q^2) = F_2^{1/Q^2}(x, Q^2) + (\rho^2 - 1)^2 \left[ \frac{23}{16} F_2^{(0)}(x, Q^2) + \frac{3x}{8} F_2^{(0)'}(x, Q^2) \right. \\ \left. + \frac{x^2}{32} F_2^{(0)''}(x, Q^2) - 3x h_2(x, Q^2) + \frac{3}{4} g_2(x, Q^2) \right], \quad (8b)$$

$$F_L^{1/Q^4}(x, Q^2) = F_L^{1/Q^2}(x, Q^2) + (\rho^2 - 1)^2 \left[ \frac{3}{16} F_L^{(0)}(x, Q^2) + \frac{1}{4} F_2^{(0)}(x, Q^2) \right. \\ \left. + \frac{x}{8} F_L^{(0)'}(x, Q^2) + \frac{x^2}{32} F_L^{(0)''}(x, Q^2) - x h_2(x, Q^2) + \frac{1}{2} g_2(x, Q^2) \right], \quad (8c)$$

$$F_3^{1/Q^4}(x, Q^2) = F_3^{1/Q^2}(x, Q^2) + (\rho^2 - 1)^2 \left[ \frac{13}{16} F_3^{(0)}(x, Q^2) + \frac{5x}{16} F_3^{(0)'}(x, Q^2) \right. \\ \left. + \frac{x^2}{32} F_3^{(0)''}(x, Q^2) - \frac{3}{4} h_3(x, Q^2) \right], \quad (8d)$$

where the first  $(F_i^{(0)'})$  and second  $(F_2^{(0)'})$  derivatives of the structure functions are with respect to  $x$ . In fact, one can show that for a structure function that behaves at large  $x$  as  $(1-x)^n$ , the target mass corrected result will vanish in the  $x \rightarrow 1$  limit up to order  $1/Q^{2n-2}$  in the expansion. For  $n \approx 3$ , as is typical for nucleon structure functions, the threshold problem will therefore appear only at order  $1/Q^6$ .

The accuracy of the  $1/Q^2$  expansions is illustrated in Fig. 1, where in order to isolate the target mass effect from the specific form of the structure function parametrization we have taken for simplicity the form  $F_2 \sim (1-x)^3$ . Both the  $1/Q^2$  and  $1/Q^4$  approximations are found to reproduce the full OPE result very well up to  $x \approx 0.6$ , but significant deviations are visible at larger  $x$ . Furthermore, while there is a modest improvement in the agreement with the exact result for  $0.6 \lesssim x \lesssim 0.8$  after inclusion of the  $1/Q^4$  terms, both expansions appear to break down for  $x \gtrsim 0.8$ . The reliability of a low order  $1/Q^2$  expansion is therefore questionable at these  $x$  values, and hence their efficacy in removing the  $x \rightarrow 1$  threshold problem.

Since the integrals in the functions  $h_{2,3}$  and  $g_2$  can be time consuming to compute numerically, Schienbein *et al.* [18] found phenomenological analytic forms which approximate

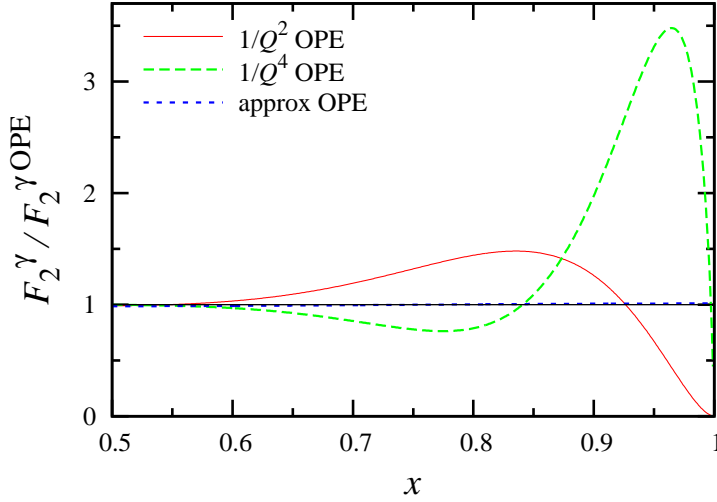


FIG. 1: Ratio of the target mass corrected  $F_2$  structure functions using the  $1/Q^2$  (solid, red),  $1/Q^4$  (long-dashed, green) and phenomenological (short-dashed, blue) OPE approximations compared with the exact OPE result, Eq. (4b). Note that the phenomenological OPE approximation is almost indistinguishable from the exact OPE result, while the  $1/Q^2$  and  $1/Q^4$  expansions deviate from this for  $x \gtrsim 0.6$ .

the target mass corrected  $F_2$  and  $F_3$  structure functions in Eqs. (4b) and (4d) by

$$F_2^{\text{approx}}(x, Q^2) = \frac{(1+\rho)^2}{2\rho^3} \left( 1 + \frac{3(\rho^2-1)}{\rho(1+\rho)}(1-\xi)^2 \right) F_2^{(0)}(\xi, Q^2), \quad (9a)$$

$$F_3^{\text{approx}}(x, Q^2) = \frac{(1+\rho)}{2\rho^2} \left( 1 - \frac{(\rho^2-1)}{2\rho(1+\rho)}(1-\xi) \ln \xi \right) F_3^{(0)}(\xi, Q^2). \quad (9b)$$

These turn out to be rather good approximations to the exact results, as Fig. 1 illustrates for the  $F_2$  case. For all values of  $x$ , the phenomenological approximation (9a) stays within 5% of the full OPE result.

## B. Collinear factorization

An alternative approach to TMCs relies on the collinear factorization (CF) formalism [19–22], which makes use of the factorization theorem to relate the hadronic tensor for lepton–hadron scattering to that for scattering from a parton. Here parton distributions are formulated directly in momentum space, avoiding the need to perform an inverse Mellin transform to obtain the PDF from its moments. An advantage of the CF formalism for TMCs is that it can be extended to other hard scattering processes, such as semi-inclusive

DIS [35], where an OPE is not available.

### 1. *Ellis, Furmanski and Petronzio*

The first study of TMCs within CF was made by Ellis, Furmanski, and Petronzio (EFP) [19], who analyzed the virtual photon-hadron scattering amplitude using a Feynman diagram technique to expand the hard scattering term about the collinear direction, incorporating both parton off-shellness (or interactions) and parton transverse momentum in twist-4 contributions [36]. Using the same notation as for the OPE TMCs above, the EFP results for the target mass corrected structure functions are given by

$$F_1^{\text{EFP}}(x, Q^2) = \frac{2}{1+\rho} F_1^{(0)}(\xi, Q^2) + \frac{(\rho^2 - 1)}{(1+\rho)^2} h_2(\xi, Q^2), \quad (10a)$$

$$F_2^{\text{EFP}}(x, Q^2) = \frac{1}{\rho^2} F_2^{(0)}(\xi, Q^2) + \frac{3\xi(\rho^2 - 1)}{\rho^2(1+\rho)} h_2(\xi, Q^2), \quad (10b)$$

$$F_L^{\text{EFP}}(x, Q^2) = F_L^{(0)}(\xi, Q^2) + \frac{2\xi(\rho^2 - 1)}{(1+\rho)} h_2(\xi, Q^2), \quad (10c)$$

$$F_3^{\text{EFP}}(x, Q^2) = \frac{1}{\rho} F_3^{(0)}(\xi, Q^2) + \frac{2(\rho^2 - 1)}{\rho(1+\rho)^2} h_3(\xi, Q^2), \quad (10d)$$

where again the  $F_i^{(0)}$  refer to the uncorrected structure functions, and  $h_{2,3}$  are given in Eqs. (6). (Note that the definition of the longitudinal structure function in EFP differs from the usual definition (2) by a factor  $x$ , and the  $F_2$  structure function is proportional to what EFP call the “transverse” structure function, which in standard usage is proportional to  $F_1$ .) Because the massless functions  $F_i^{(0)}$  are evaluated at  $\xi$ , the target mass corrected structure functions will suffer from the same threshold problem as in the OPE analysis in Eqs. (4). While the expressions in Eqs. (10) were derived in Ref. [19] at leading order in  $\alpha_s$ , in this work we will assume their validity also at NLO.

The prefactors for the leading terms proportional to  $F_i^{(0)}$  in Eqs. (10) are remarkably close to those for the leading terms in the OPE expressions in Eqs. (4). To first order in  $1/Q^2$ , the leading term prefactors for  $F_1$  in both OPE and EFP reduce to  $(1 - x^2 M^2/Q^2)$ . Similarly, the  $F_2$  prefactors both reduce to  $(1 - 4x^2 M^2/Q^2)$ , while those for  $F_L$  reduce to 1. For the  $F_3$  structure function, however, the  $\mathcal{O}(1/Q^2)$  prefactor is  $(1 - 3x^2 M^2/Q^2)$  for OPE, whereas for the EFP CF result it is  $(1 - 2x^2 M^2/Q^2)$ .

At leading order in the massless limit the longitudinal structure function vanishes identically. At NLO, however, it receives contributions from both quark and gluon PDFs con-

volved with the respective hard coefficient functions. For electromagnetic scattering, for example, one has [37, 38]

$$F_L^{\gamma(0)}(x, Q^2) = \frac{\alpha_s(Q^2)}{\pi} \int_x^1 \frac{dy}{y} \left(\frac{x}{y}\right)^2 \left\{ \frac{4}{3} F_2^{\gamma(0), \text{LO}}(y, Q^2) + c^\gamma(y-x)g(y, Q^2) \right\}, \quad (11)$$

where  $c^\gamma = 2 \sum_q e_q^2$ , and  $F_2^{\gamma(0), \text{LO}}$  is given by the leading order expression for  $F_2^{\gamma(0)}$ . Similar expressions hold also for the longitudinal structure functions associated with other electroweak currents. In our numerical calculations discussed below we will always compute  $F_L$  at NLO.

It is important also to note that Eqs. (10) have been derived considering Feynman diagrams with 2 or 4 legs attached to the hadronic correlator (see Figs. 2 and 3 of Ref. [19]), which for  $M = 0$  give rise to twist-2 and twist-4 contributions to the structure functions, respectively. For  $M \neq 0$ , however, the quark and gluon equations of motion allow one to extract a twist-2 contribution from the 4-leg diagrams, which when added to the twist-2 target mass correction yields the full result in Eqs. (10). It is an interesting question whether by resumming the twist-2 parts of  $n$ -leg diagrams one would be able to recover the TMC expressions (10).

## 2. Accardi and Qiu

In both the EFP and OPE treatments of TMCs, the resulting structure functions are nonzero for  $x > 1$ . The analysis of Accardi and Qiu (AQ) [22] traced this problem to baryon number nonconservation in the handbag diagram for  $M \neq 0$ . Working with 2-leg diagrams only, in contrast to EFP who also consider 4-leg diagrams up to twist-4, the AQ target mass corrected structure functions are given by [22]

$$F_1^{\text{AQ}}(x, Q^2) = \tilde{F}_1^{(0)}(\xi, Q^2), \quad (12a)$$

$$F_2^{\text{AQ}}(x, Q^2) = \frac{1+\rho}{2\rho^2} \tilde{F}_2^{(0)}(\xi, Q^2), \quad (12b)$$

$$F_L^{\text{AQ}}(x, Q^2) = \frac{1+\rho}{2} \tilde{F}_L^{(0)}(\xi, Q^2), \quad (12c)$$

$$F_3^{\text{AQ}}(x, Q^2) = \frac{1}{\rho} \tilde{F}_3^{(0)}(\xi, Q^2). \quad (12d)$$

Here the functions  $\tilde{F}_i^{(0)}$  are defined as

$$\tilde{F}_i^{(0)}(\xi, Q^2) = \sum_f \int_\xi^{\xi/x} \frac{dz}{z} C_i^f\left(\frac{\xi}{z}, Q^2\right) \varphi_f(z, Q^2), \quad (13)$$

where  $C_i^f$  are the perturbatively calculable hard coefficient functions for a given parton flavor  $f$ , including parton charge factors,  $\varphi_f$  are the parton densities of the nucleon, and the sum is taken over all active flavors. The upper limit in Eq. (13) ensures that the target mass corrected structure functions vanish for  $x > 1$ , as required by kinematics, although jet mass corrections need to be introduced in order to render the target mass corrected functions zero at  $x = 1$  [22]. It remains an interesting exercise to apply the same prescription to twist-4 diagrams as in Ref. [19] in order to establish a more direct correspondence between the AQ and EFP approaches. Of course, for  $M^2/Q^2 \rightarrow 0$  the upper limit of integration in Eq. (13) is 1, and both approaches recover the standard factorization theorem for structure functions [39].

### 3. $\xi$ -scaling

When the upper limit of integration in Eq. (13) is taken to be 1, the AQ structure functions reduce to the simple  $\xi$ -scaling ( $\xi$ -S) form introduced by Aivazis *et al.* [20] and used by Kretzer and Reno [21]. The target mass corrected structure functions in this case are simply given by

$$F_1^{\xi\text{-S}}(x, Q^2) = F_1^{(0)}(\xi, Q^2), \quad (14a)$$

$$F_2^{\xi\text{-S}}(x, Q^2) = \frac{1+\rho}{2\rho^2} F_2^{(0)}(\xi, Q^2), \quad (14b)$$

$$F_L^{\xi\text{-S}}(x, Q^2) = \frac{1+\rho}{2} F_L^{(0)}(\xi, Q^2), \quad (14c)$$

$$F_3^{\xi\text{-S}}(x, Q^2) = \frac{1}{\rho} F_3^{(0)}(\xi, Q^2). \quad (14d)$$

Note that the form of the target mass corrected functions in Eqs. (14) closely resembles that in Eqs. (12), with the two forms equivalent at leading order. At this order the structure functions satisfy a modified Callan-Gross relation [22],

$$\rho^2 F_2^{\xi\text{-S}}(x, Q^2) = 2x F_1^{\xi\text{-S}}(x, Q^2). \quad (15)$$

The leading order  $\xi$ -scaling structure functions are also related to the leading,  $\mathcal{O}(1)$  terms of the OPE expressions in Eqs. (4),

$$F_i^{\text{OPE (leading)}}(\xi, Q^2) = \frac{1+\rho}{2\rho} F_i^{\xi\text{-S}}(\xi, Q^2), \quad (16)$$

where the prefactor, to order  $1/Q^2$ , is given by  $(1 - x^2 M^2/Q^2)$ . In fact, the  $\xi$ -scaling formulas (14) would coincide with the EFP results in Sec. IIB1 in the absence of 4-leg Feynman diagrams [19].

### C. TMC comparisons

The effects of the different TMC prescriptions on structure functions are illustrated in Figs. 2 – 5 for the  $F_1^\gamma$ ,  $F_2^\gamma$ ,  $F_L^\gamma$  and  $F_3^{W^+}$  structure functions of the proton, respectively. (The results for structure functions associated with other boson exchanges, such as  $W^-$ ,  $Z$ , or  $\gamma Z$  interference, are very similar to these.) The uncorrected proton structure functions  $F_i^{(0)}$  are constructed from the CTEQ-Jefferson Lab (CJ) global PDF fits [7], evaluated at  $Q^2 = 2 \text{ GeV}^2$ . For each of the structure functions the effects of TMCs become more prominent with increasing  $x$ , and naturally their magnitude decreases at larger  $Q^2$ .

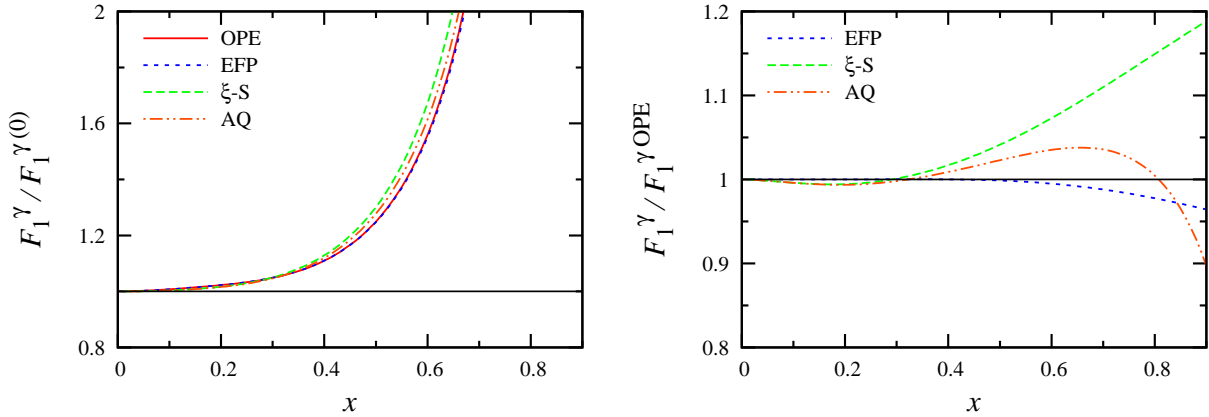


FIG. 2: Ratio of target mass corrected to uncorrected (**left**) or to OPE (**right**)  $F_1^\gamma$  proton structure functions at  $Q^2 = 2 \text{ GeV}^2$  for the OPE (solid, red), EFP (short-dashed, blue),  $\xi$ -S (long-dashed, green), and AQ (dot-dashed, orange) TMC prescriptions. Note that the OPE and EFP results are almost indistinguishable for  $x \lesssim 0.6$ .

For the  $F_1^\gamma$  structure function in Fig. 2, the deviation from unity of the ratio of target mass corrected to uncorrected functions ranges from  $\sim 10\%$  at  $x = 0.4$ , to more than a factor 2 for  $x \gtrsim 0.7$ . The model dependence of the TMCs to  $F_1^\gamma$  is relatively weak; the OPE [17] and EFP [19] results are similar to within a few percent for all  $x$ , while the  $\xi$ -scaling [20, 21] and AQ [22] prescriptions differ from the OPE by  $\lesssim 5\%$  and  $15\%$ , respectively, for  $x \lesssim 0.8$ . (Results for  $x \gtrsim 0.9$  are not shown as the input nucleon PDFs are not constrained

in this region and display numerical instability at  $x \gtrsim 0.95$ .) In fact, at low and moderate  $x$  the OPE and EFP TMCs track each other rather closely, as expected from the equality of their leading term prefactors at order  $1/Q^2$ . Similarly, the AQ and  $\xi$ -scaling prescriptions are much closer to each other than to the OPE and EFP results, as may be anticipated from the structure of the respective TMC expressions in Eqs. (12) and (14).

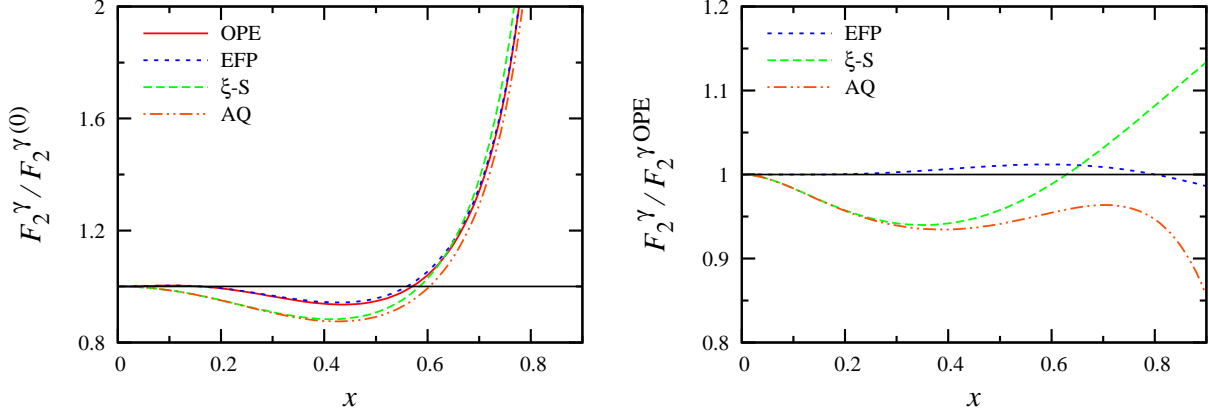


FIG. 3: As in Fig. 2, but for the  $F_2^\gamma$  proton structure function.

Qualitatively similar behavior is seen also for the target mass corrected  $F_2^\gamma$  structure function in Fig. 3. Here a dip in the ratio of corrected to uncorrected functions at  $x \sim 0.4$ , however, delays the sharp rise above unity to  $x \gtrsim 0.6$ . As for  $F_1^\gamma$ , the EFP result agrees with the OPE to a few percent over the entire  $x$  range, and the AQ and  $\xi$ -scaling ratios are almost identical for  $x < 0.4$ . The two sets of ratios differ by  $\lesssim 7\%$  for  $x < 0.7$ , before diverging somewhat as  $x \rightarrow 1$ .

For the  $F_L^\gamma$  structure function in Fig. 4 the differences between the various TMC prescriptions are more dramatic. The OPE and EFP ratios begin to rise steeply at low  $x$ , with the corrected functions exceeding the uncorrected ones by more than a factor 5 already by  $x = 0.5$ . The AQ and  $\xi$ -S ratios, on the other hand, rise above unity at much higher  $x$ , reminiscent of the  $F_1$  ratios in Fig. 2. The two sets of corrections differ by more than 50% by  $x = 0.3$ , and by  $\gtrsim 80\%$  for  $x > 0.8$ . This qualitatively rather different behavior can be understood by directly comparing Eqs. (4) and (10) to Eqs. (12) and (14). Unlike the  $\xi$ -S and AQ prescriptions, the OPE and EFP  $F_L$  results include terms involving integrals over  $F_2$ , which is generally  $\gg F_L$ . In fact, to leading order with no TMCs, the  $F_L$  structure function vanishes, and adding NLO corrections within the AQ or  $\xi$ -S prescriptions does not produce a significant increase. In contrast, the OPE and EFP prescriptions always receive

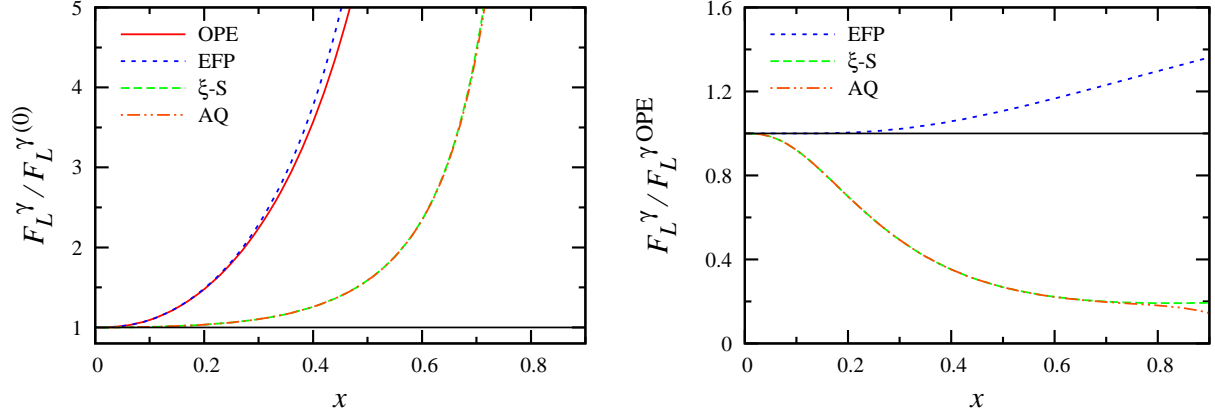


FIG. 4: As in Fig. 2, but for the  $F_L^\gamma$  proton structure function.

large  $F_2$  contributions, making the target mass corrected to uncorrected ratio considerably larger in these approaches.

The strong correlations between the OPE and EFP predictions are not as visible for the  $F_3$  structure function, which, unlike the other structure functions, differs already at  $\mathcal{O}(1/Q^2)$ . The general shape of the TMC ratio, illustrated in Fig. 5 for the  $F_3^{W^+}$  structure function, resembles that for  $F_2^\gamma$  in Fig. 3, but with a rise above unity beginning at lower  $x$ . The various prescriptions agree to  $\sim 10\%$  for  $x \lesssim 0.4$ , and  $\sim 40\%$  for  $x \lesssim 0.8$ , but generally display more spread than in  $F_1^\gamma$  or  $F_2^\gamma$ .

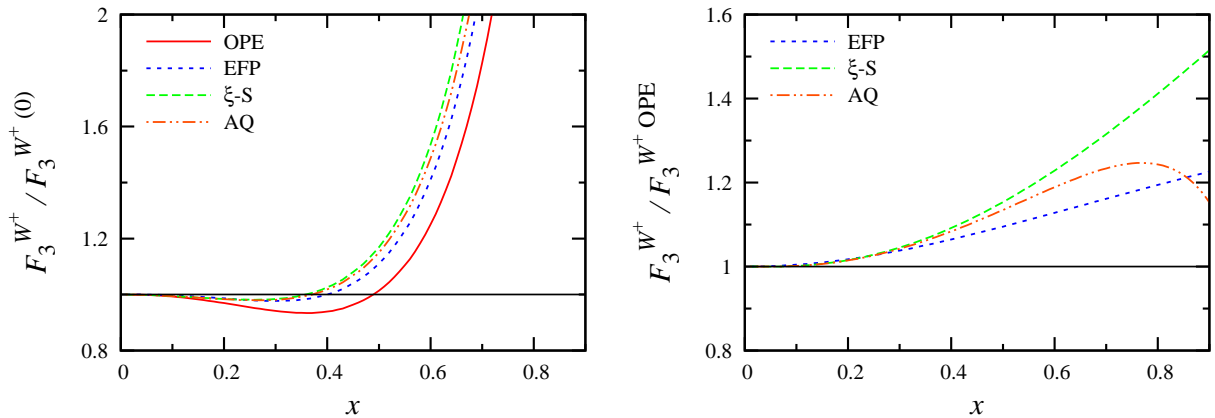


FIG. 5: As in Fig. 2, but for the  $F_3^{W^+}$  proton structure function.

### III. IMPLICATIONS FOR OBSERVABLES

Having examined the differences between the various TMC prescriptions on individual structure functions, in this section we consider the effects of TMCs, and in particular their model dependence, on several observables that will be measured in upcoming experiments. These include the ratio of the neutron to proton  $F_2$  structure functions, the longitudinal to transverse (LT) cross section ratios, and parity-violating deep-inelastic scattering asymmetries for the proton and deuteron.

#### A. Neutron to proton ratio

Historically, the ratio of  $d$  to  $u$  quark distributions in the proton has been determined primarily through the ratio of neutron to proton electromagnetic DIS cross sections,

$$R_{np} = \frac{d^2\sigma^{\gamma n}/dxdy}{d^2\sigma^{\gamma p}/dxdy} = \frac{F_2^{\gamma n}}{F_2^{\gamma p}} \left( \frac{1 - y - y^2 [\rho^2 - 1 - 2\rho^2/(1 + R^{\gamma n})] / 4}{1 - y - y^2 [\rho^2 - 1 - 2\rho^2/(1 + R^{\gamma p})] / 4} \right), \quad (17)$$

where  $y = \nu/E$  is the fractional energy transfer from the lepton, and  $R^{\gamma N}$  is the ratio of the longitudinal to transverse cross sections, or structure functions,

$$R^{\gamma N} = \frac{F_L^{\gamma N}}{2xF_1^{\gamma N}} \quad (18)$$

for nucleon  $N$ . With the assumption that  $R^{\gamma n} = R^{\gamma p}$ , the ratio of cross sections becomes the ratio of  $F_2$  structure functions,  $R_{np} \rightarrow F_2^{\gamma n}/F_2^{\gamma p}$ . To leading order, the ratio (17) is then given by  $R_{np} = (1 + 4d/u)/(4 + d/u)$ , which illustrates the sensitivity to the  $d/u$  PDF ratio. In practice, differences between  $R^{\gamma p}$  and  $R^{\gamma n}$  generated perturbatively at NLO have a negligible effect on the ratio  $R_{np}$  at the kinematics considered here.

The absence of free neutron targets has meant that in practice inclusive deuterium structure function data has been used to obtain indirect information on the neutron, and hence the  $d$  quark. This procedure is known to suffer from significant model dependence at large values of  $x$  [7, 40, 41], leading to several novel new experiments being proposed [11–13] to determine the  $d/u$  ratio with minimal nuclear model uncertainties. In order for these measurements to be unambiguously analyzed, it is important to quantify the extent of TMC uncertainties at the kinematics of the experiments, which will typically reach a maximum  $Q^2 \sim 10 - 15 \text{ GeV}^2$  at  $x \approx 0.8$ .

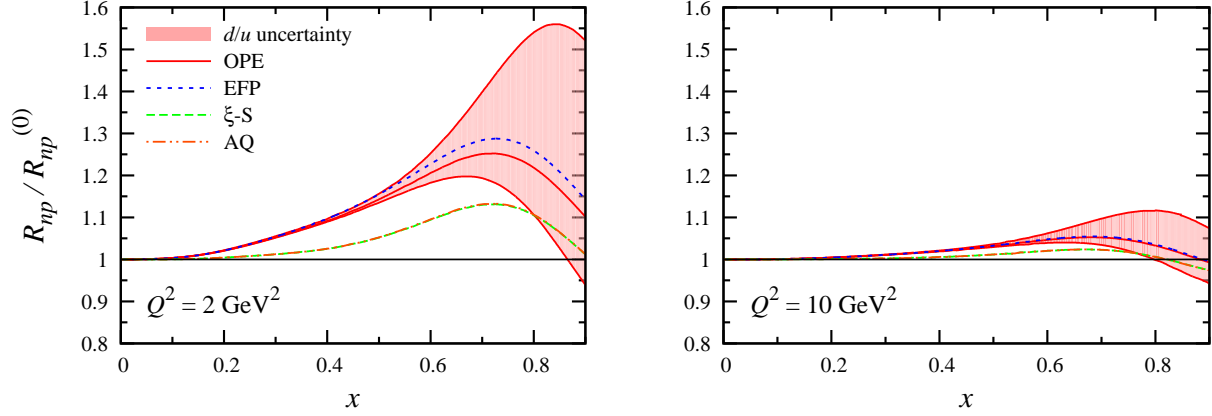


FIG. 6: Ratio of target mass corrected ( $R_{np}$ ) to uncorrected ( $R_{np}^{(0)}$ ) neutron to proton  $F_2$  structure function ratios at  $Q^2 = 2 \text{ GeV}^2$  (**left**) and  $Q^2 = 10 \text{ GeV}^2$  (**right**), for the OPE (solid, red), EFP (short-dashed, blue),  $\xi$ -S (long-dashed, green), and AQ (dot-dashed, orange) TMC prescriptions. The shaded band represents the uncertainty in the ratio  $d/u$  for the OPE result. Note that the AQ and  $\xi$ -S results are almost identical.

The effects of TMCs on the ratio  $R_{np}$  are illustrated in Fig. 6 for the CJ PDFs [7] at  $Q^2 = 2 \text{ GeV}^2$  (left) and  $10 \text{ GeV}^2$  (right). The shaded bands represent the  $d/u$  uncertainty range as applied to the OPE TMC prescription, with the central solid (red) curve denoting the median value for OPE calculated with the same PDFs as the other TMC prescriptions. The target mass corrections at  $Q^2 = 2 \text{ GeV}^2$  are sizable, reaching  $\approx 25\% - 30\%$  at  $x = 0.7$  for the OPE and EFP prescriptions, and  $\approx 12\%$  for the  $\xi$ -S and AQ results. At the higher  $Q^2 = 10 \text{ GeV}^2$  value the TMCs decrease to  $\approx 5\%$  and  $\approx 2\%$  for the OPE/EFP and  $\xi$ -S/AQ calculations, respectively. Treating each of the TMC prescriptions on equal footing, this would suggest an uncertainty due to TMCs of  $\lesssim 3\%$  for all values of  $x$  accessible in the planned experiments [11–13].

The TMC uncertainty can be compared with the range of  $R_{np}$  predicted from PDFs extracted under different assumptions about the size of nuclear corrections in deuterium, which currently represents the largest uncertainty in the  $d/u$  ratio at  $x \gtrsim 0.5$  [7]. This is illustrated in the bands in Fig. 6, which represent the  $R_{np}$  ratio evaluated from the range of CJ PDFs [7] for the OPE TMC prescription. The results show that for  $Q^2 = 2 \text{ GeV}^2$  the uncertainty resulting from nuclear corrections is some 2–3 times larger than that associated with TMCs at  $x = 0.8$ . Both the uncertainties in the  $d$  quark PDF and in the TMCs decrease as  $x$  decreases, albeit more slowly for the latter. At  $x = 0.6$ , in fact, the two uncertainties

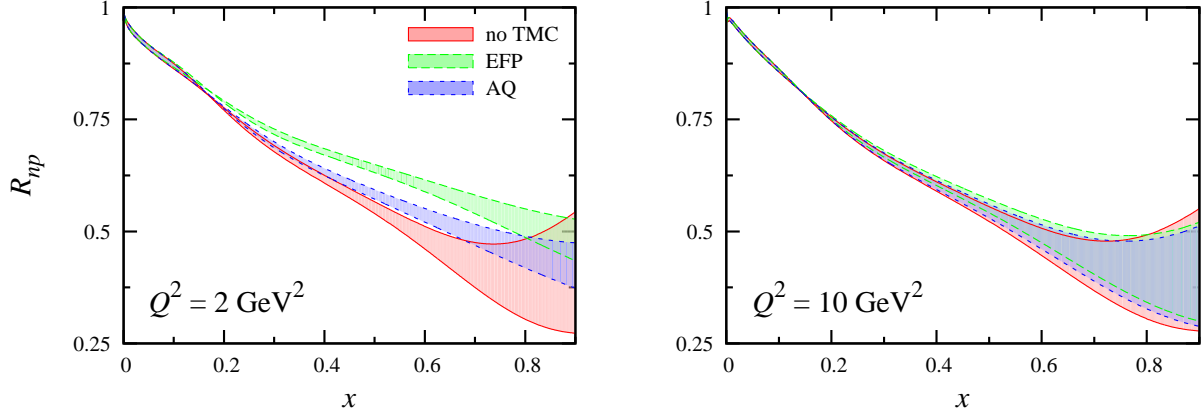


FIG. 7: Neutron to proton  $F_2$  structure function ratio  $R_{np}$  at  $Q^2 = 2 \text{ GeV}^2$  (**left**) and  $Q^2 = 10 \text{ GeV}^2$  (**right**), with the shaded bands representing the  $d/u$  uncertainty for uncorrected structure functions (solid, red) and the two extremal TMCs, EFP (long-dashed, green) and AQ (short-dashed, blue).

are comparable, while for  $x \lesssim 0.4$  the TMC uncertainty is actually larger.

With increasing  $Q^2$  both the TMCs and their uncertainties decrease, while the uncertainty in the leading twist PDFs remains approximately  $Q^2$  independent, as can be seen more clearly in the comparison of the absolute values of  $R_{np}$  in Fig. 7. At  $Q^2 = 2 \text{ GeV}^2$  the bands representing the  $R_{np}$  ratio evaluated from the CJ PDFs [7] using different TMC prescriptions (specifically the extremal EFP and AQ results) do not overlap until  $x \sim 0.75$ , meaning that at smaller  $x$  the true  $d/u$  behavior will be obscured by the relatively large TMC model uncertainty. Interestingly, the TMCs actually *decrease* the nuclear uncertainty range at lower  $Q^2$ , since the action of the  $x \rightarrow \xi$  rescaling is to effectively feed information from lower  $x$  in the uncorrected functions (which have relatively small  $d/u$  uncertainty) to higher  $x$  values (where the  $d/u$  uncertainty is larger). Consequently, at higher  $Q^2$  the sensitivity to the  $d/u$  ratio increases both due to the smaller spread of results for different TMC prescriptions, and to the weakening of the TMC effect in moving strength from lower  $x$  for a particular TMC prescription. This is indeed visible in Fig. 7 for the  $R_{np}$  ratio at  $Q^2 = 10 \text{ GeV}^2$ , in which the EFP and AQ extremal TMC bands very nearly coincide over the entire  $x$  range, as well as with the ratio computed without TMCs. Such values of  $Q^2$  will therefore be required in order to cleanly extricate the  $d/u$  ratio from measurements of the neutron to proton ratio without ambiguities associated with TMC model dependence.

Finally, we also note that in global QCD fits of PDFs it was recently found [6] that the

impact of the model dependence of TMCs on leading twist PDFs is reduced significantly with the inclusion of a phenomenological  $1/Q^2$  higher twist term in the  $F_2$  structure function parametrization, with the two effects partially compensating each other. Since the higher twist contribution to  $F_L$  is independent of that for  $F_2$ , a similar cancellation may be expected also when including  $F_L$  data in the global fits. The uncertainties in extracted PDFs induced by the model dependence of TMCs may therefore be smaller than those suggested in Fig. 6 if the data are analyzed within a global PDF context.

### B. Longitudinal to transverse structure function ratios

While the LT cross section ratio  $R^{\gamma N}$  is expected to play a relatively minor role in the measurements of the neutron to proton  $F_2$  structure function ratio in Eq. (17), mostly because of the cancellation between the proton and neutron  $R^{\gamma N}$  values, the effects of TMCs on the ratio itself may be more significant. This was already suggested by the large prescription dependence of TMCs for the longitudinal structure function  $F_L^\gamma$  in Fig. 4. The effects of TMCs on the LT ratio are also important to quantify in connection with establishing the low- $Q^2$  behavior of  $R^{\gamma N}$  at finite  $x$ , to determine the onset of gauge invariance constraints on the longitudinal structure function [42].

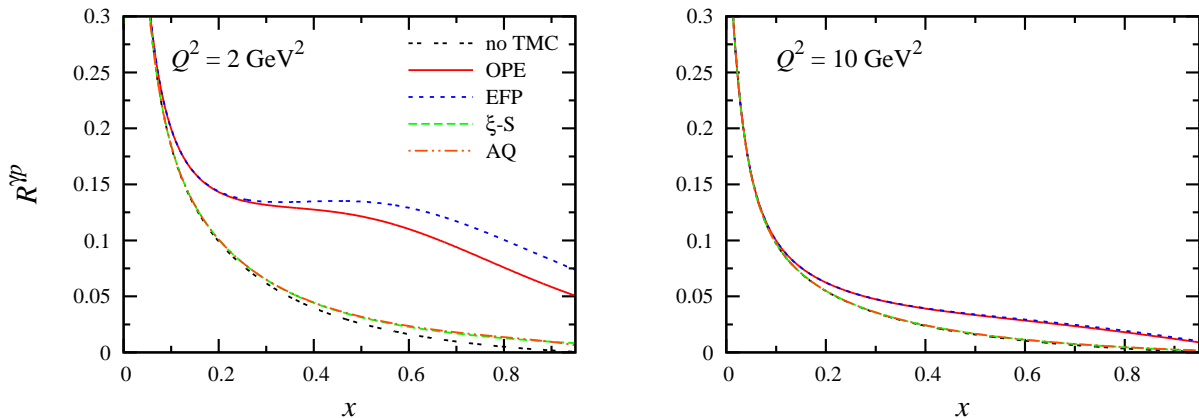


FIG. 8: Longitudinal to transverse cross section ratio  $R^{\gamma p}$  for the proton at  $Q^2 = 2 \text{ GeV}^2$  (**left**) and  $Q^2 = 10 \text{ GeV}^2$  (**right**), for no TMCs (double-dashed, black), the OPE (solid, red), EFP (short-dashed, blue),  $\xi$ -S (long-dashed, green), and AQ (dot-dashed, orange) TMC prescriptions.

In Fig. 8 we illustrate the TMC effects on  $R^{\gamma p}$  for  $Q^2 = 2$  and  $10 \text{ GeV}^2$  for each of the TMC prescriptions considered. All of the TMCs increase the magnitude of the  $R^{\gamma p}$  ratio,

with the AQ and  $\xi$ -S prescriptions having a relatively modest effect (approximately a factor 2 for  $x \approx 0.6 - 0.8$  at  $Q^2 = 2 \text{ GeV}^2$ , but only a few percent at  $Q^2 = 10 \text{ GeV}^2$ ), while the EFP and OPE both altering the ratio significantly for  $x \gtrsim 0.1$ . The enhancement of  $R^{\gamma p}$  for the latter is predicted to be about an order of magnitude for  $x \approx 0.6 - 0.8$  at  $Q^2 = 2 \text{ GeV}^2$ , and still a factor of 3 – 4 at  $Q^2 = 10 \text{ GeV}^2$ .

Some differences are also expected between the longitudinal to transverse cross section ratios at NLO for processes involving electromagnetic and weak currents. In particular, as will be discussed in more detail in Sec. III C below, asymmetries measured in parity-violating electron scattering are sensitive to interference effects between  $\gamma$  and  $Z$  boson exchange, and differences between the  $R^\gamma$  and  $R^{\gamma Z}$  LT ratios can affect the measured asymmetries [23, 24].

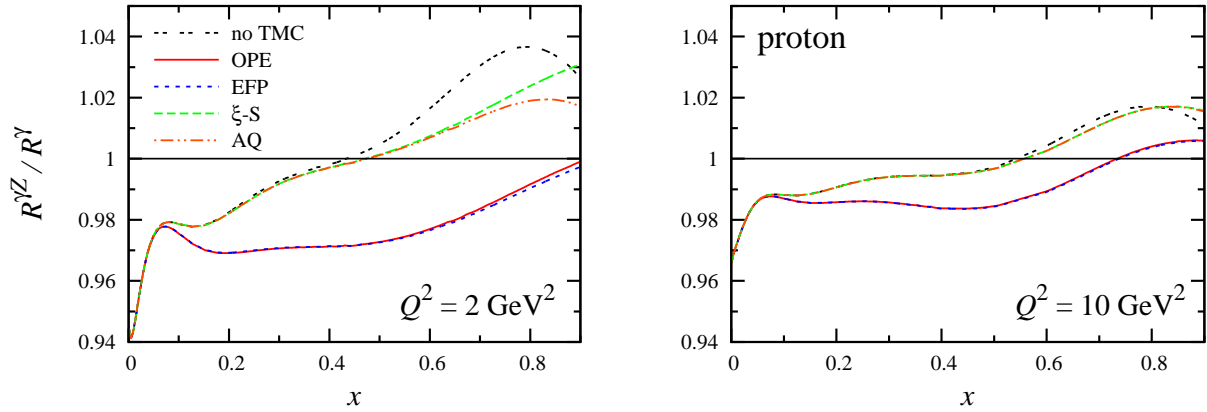


FIG. 9: Ratio of  $R^{\gamma Z}$  to  $R^\gamma$  LT ratios for the *proton* computed at NLO for  $Q^2 = 2 \text{ GeV}^2$  (**left**) and  $Q^2 = 10 \text{ GeV}^2$  (**right**), for no TMCs (double-dashed, black), the OPE (solid, red), EFP (short-dashed, blue),  $\xi$ -S (long-dashed, green), and AQ (dot-dashed, orange) TMC prescriptions.

In Fig. 9 the ratio of the proton  $R^{\gamma Z}$  to  $R^\gamma$  LT ratios is shown at  $Q^2 = 2$  and  $10 \text{ GeV}^2$ . While at leading order both of these ratios are zero, at NLO the different relative contributions from quark PDFs to the electromagnetic and  $\gamma Z$  interference structure functions leads to deviations of the ratios from unity of up to  $\approx 4\%$  at  $Q^2 = 2 \text{ GeV}^2$ , and up to  $\approx 2\%$  at  $Q^2 = 10 \text{ GeV}^2$ . The effects of the TMCs are again very small for the  $\xi$ -scaling and AQ prescriptions, but more significant for the OPE and EFP results. Overall, the spread in the TMC predictions for the  $R^{\gamma Z}/R^\gamma$  ratio amounts to  $\lesssim 4 - 5\%$  for  $x$  between 0.6 and 0.8 at  $Q^2 = 2 \text{ GeV}^2$ , and  $\lesssim 2\%$  at  $Q^2 = 10 \text{ GeV}^2$ . Note that the dip in the ratios at  $x < 0.1$ , which is insensitive to TMCs, reflects the greater role played by gluons at low  $x$ , but is mostly irrelevant for the kinematics of the proposed experiments [11–13].

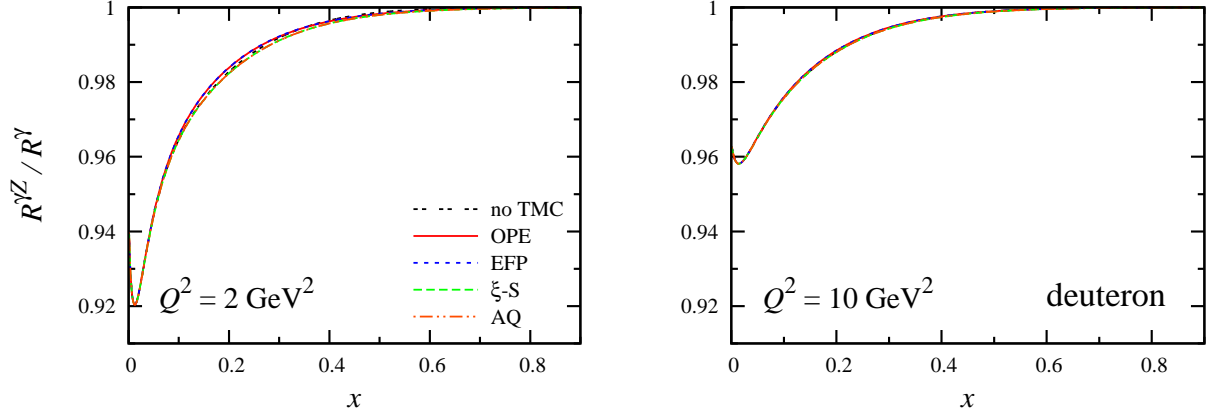


FIG. 10: As in Fig. 9, but for the *deuteron*  $R^{\gamma Z}$  to  $R^{\gamma}$  LT ratio.

For the case of the isoscalar deuteron target, stronger cancellations between the quark content of  $R^{\gamma Z}$  and  $R^{\gamma}$  are expected to lead to smaller deviations of their ratio from unity at large  $x$ . This is indeed observed in Fig. 10, where again the dip in the ratio at very low  $x$  is associated with NLO gluon dominance of the LT ratios as  $x \rightarrow 0$ . At  $x = 0.2$ , for example, the gluonic content of  $F_L$  suppresses the deuteron  $R^{\gamma Z}/R^{\gamma}$  ratio by  $\approx 2\%$  for  $Q^2 = 2 \text{ GeV}^2$ , and  $\approx 1\%$  for  $Q^2 = 10 \text{ GeV}^2$ . At higher  $x$  the deviations decrease until the ratio approaches unity asymptotically as  $x \rightarrow 1$ . In the region of  $x$  where the LT ratios are dominated by quarks, the fact that the same isoscalar combination of quark PDFs enters both the electromagnetic and  $\gamma Z$  interference structure functions leads to almost negligible TMC effects. The absence of significant TMC effects in the deuteron ratio is, as expected, even more clearly visible at the higher  $Q^2$  value.

Finally, for experiments involving deuteron targets one needs to account for the fact that the nucleons in the nucleus are bound and hence have structure functions that differ from those of free nucleons. In Fig. 11 the LT ratio  $R^{\gamma Z}$  for the  $\gamma Z$  interference structure functions of the deuteron is shown relative to that for a free isoscalar nucleon (defined as proton + neutron) at  $Q^2 = 2 \text{ GeV}^2$ , using the nuclear smearing model of Refs. [34, 43] (see also Ref. [7]). The shape of the deuteron to nucleon ratio computed at NLO in the absence of TMCs displays a dramatic rise above unity with increasing  $x$  that is characteristic of the nuclear EMC ratio [44]. The effects of Fermi motion in fact lead to a divergent ratio at  $x = 1$ . The inclusion of TMCs suppresses the rise at large  $x$ , from  $\approx 60\%$  at  $x = 0.6$  to  $20\%$  for the  $\xi$ -scaling and AQ prescriptions, and to  $\approx 5\%$  for the OPE and EFP cases, with larger differences as  $x \rightarrow 1$ . This suppression arises because TMCs shift strength in  $F_L$  from

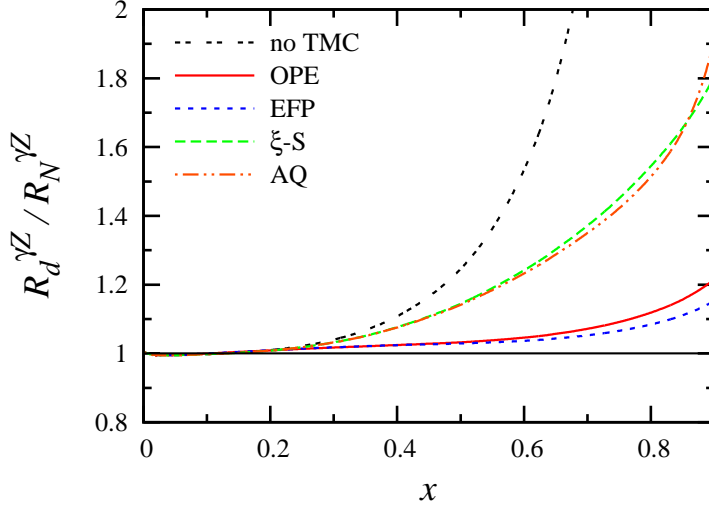


FIG. 11: Ratio of the NLO  $R^{\gamma Z}$  LT ratios for the deuteron and isoscalar nucleon ( $N = p + n$ ) at  $Q^2 = 2 \text{ GeV}^2$  for no TMCs (double-dashed, black) and the OPE (solid, red), EFP (short-dashed, blue),  $\xi$ -S (long-dashed, green), and AQ (dot-dashed, orange) TMC prescriptions.

small  $x$  to large  $x$ , thereby lessening the impact of the nuclear smearing. Since the TMC effects in the OPE and EFP prescriptions are larger than that for the  $\xi$ -S and AQ cases (see Fig. 4), the nuclear corrections for the former in Fig. 11 are smaller.

The smearing corrections to the electromagnetic LT ratio  $R^\gamma$  are almost identical to those in Fig. 11. Consequently, the net effect on the ratio  $R^{\gamma Z}/R^\gamma$  for the deuteron computed with or without nuclear corrections is  $\lesssim 0.05\%$ , and can be neglected for the kinematics of interest.

### C. Parity-violating DIS

Measurements of parity-violating deep-inelastic scattering (PVDIS) asymmetries on the proton have been proposed at Jefferson Lab [13] to provide independent constraints on the ratio of  $d/u$  quark distributions at large  $x$ , free of the nuclear correction uncertainties associated with deuterium measurements [45]. In the case of deuteron targets, where much of the dependence on hadron structure effects cancels, PVDIS asymmetries are sensitive to several effects, including charge symmetry violation in PDFs [46], or to Standard Model parameters whose precise measurement can reveal signals for new physics [25, 47]. In this section we examine the effects of TMCs on the PVDIS asymmetries of the proton and deuteron, and discuss the phenomenological implications of their uncertainties on future

planned experiments.

The PV asymmetry is defined through the difference and sum of the inclusive cross sections for scattering either a right-handed ( $R$ ) or left-handed ( $L$ ) electron from an unpolarized target,

$$A_{\text{PV}} = \frac{\sigma_R - \sigma_L}{\sigma_R + \sigma_L}, \quad (19)$$

where  $\sigma_{R,L} \equiv (d^2\sigma/d\Omega dE')_{R,L}$ . Since the purely electromagnetic and purely weak contributions to the cross section are independent of electron helicity for  $Q^2 \ll M_Z^2$ , they cancel in the numerator, leaving only the  $\gamma Z$  interference term. The denominator, on the other hand, contains all contributions, but is dominated by the purely electromagnetic component. In terms of structure functions, the asymmetry can be written [23]

$$A_{\text{PV}} = - \left( \frac{G_F Q^2}{2\sqrt{2}\pi\alpha} \right) \left[ g_A^e Y_1 \frac{F_1^{\gamma Z}}{F_1^\gamma} + \frac{g_V^e}{2} Y_3 \frac{F_3^{\gamma Z}}{F_1^\gamma} \right], \quad (20)$$

where  $g_A^e = -1/2$  and  $g_V^e = -1/2 + 2\sin^2\theta_W$  are the axial and vector couplings of the  $Z$  boson to the electron, with  $\theta_W$  the weak mixing angle, and the functions  $Y_{1,3}$  parametrize the dependence on  $y$  and on the  $R^\gamma$  and  $R^{\gamma Z}$  ratios,

$$Y_1 = \frac{1 + (1-y)^2 - y^2[1 + \rho^2 - 2\rho^2/(R^{\gamma Z} + 1)]/2}{1 + (1-y)^2 - y^2[1 + \rho^2 - 2\rho^2/(R^\gamma + 1)]/2} \left( \frac{1 + R^{\gamma Z}}{1 + R^\gamma} \right), \quad (21a)$$

$$Y_3 = \frac{1 - (1-y)^2}{1 + (1-y)^2 - y^2[1 + \rho^2 - 2\rho^2/(R^\gamma + 1)]/2} \left( \frac{\rho^2}{1 + R^\gamma} \right). \quad (21b)$$

In the limit of  $Q^2 \rightarrow \infty$ , where  $\rho \rightarrow 1$  and  $R^{\gamma, \gamma Z} \rightarrow 0$ , the kinematical factors simplify to  $Y_1 \rightarrow 1$  and  $Y_3 \rightarrow [1 - (1-y)^2]/[1 + (1-y)^2]$ .

### 1. Proton asymmetry

The proton PVDIS asymmetry is shown in Fig. 12 for  $Q^2 = 2$  and  $10 \text{ GeV}^2$  in the form of the ratio of the target mass corrected to uncorrected asymmetries. For all prescriptions the TMC effects are maximal at  $x \approx 0.7$ , where they are of the order of  $3 - 4\%$  at  $Q^2 = 2 \text{ GeV}^2$  and  $\lesssim 1\%$  at  $Q^2 = 10 \text{ GeV}^2$ . The results are slightly higher for the  $\xi$ -S and AQ corrections (which are virtually indistinguishable) than for the OPE and EFP (which are also almost identical). The small size of the effects is principally due to the strong cancellation of the TMCs in the  $F_1$  structure functions, namely,  $(F_1^{\gamma Z}/F_1^\gamma)^{\text{TMC}} \approx (F_1^{\gamma Z}/F_1^\gamma)^{(0)}$ , even though

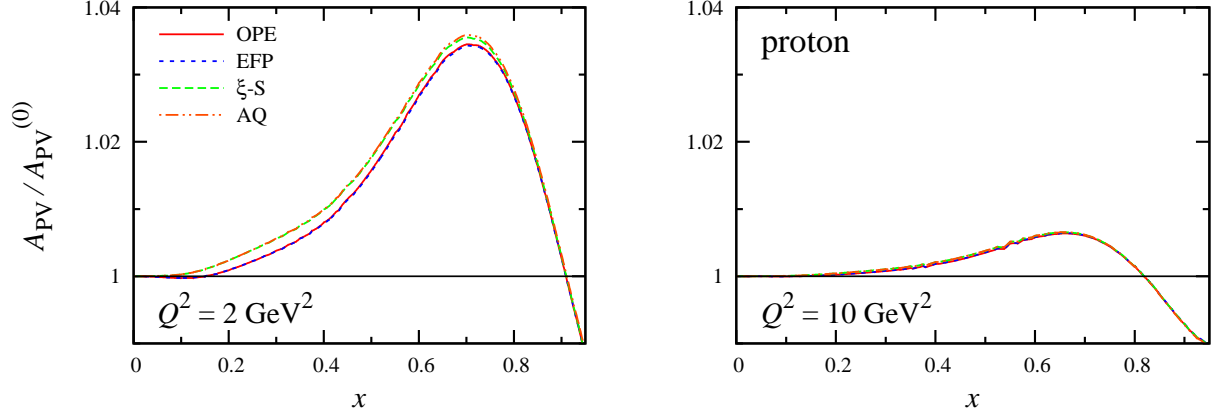


FIG. 12: Ratio of target mass corrected ( $A_{\text{PV}}$ ) to uncorrected ( $A_{\text{PV}}^{(0)}$ ) PVDIS asymmetries for the *proton* at  $Q^2 = 2 \text{ GeV}^2$  (**left**) and  $Q^2 = 10 \text{ GeV}^2$  (**right**), for the OPE (solid, red), EFP (short-dashed, blue),  $\xi$ -S (long-dashed, green), and AQ (dot-dashed, orange) TMC prescriptions. Note that the AQ and  $\xi$ -S results are almost indistinguishable, as are the EFP and OPE prescriptions.

$|F_1^{\text{TMC}}/F_1^{(0)}| \gg 1$  at high  $x$ . Overall, the results indicate that the asymmetries themselves are less sensitive to TMCs than are the LT ratios  $R^{\gamma, \gamma^* Z}$  on which the asymmetries depend.

Since one of the main goals of the proton PVDIS measurements will be to reduce the uncertainties on PDFs at large  $x$ , particularly on the  $d/u$  ratio, it is instructive to compare the magnitude of the TMC effects with the expected sensitivity of the asymmetry to different possible PDF behaviors at large  $x$ . In Fig. 13 we show the proton asymmetry  $A_{\text{PV}}$  computed from the full range of CJ PDFs [7] including minimal and maximal nuclear corrections (shaded bands) relative to the central PDF fits. The uncertainty band increases with increasing  $x$ , reflecting the larger uncertainty on the  $d$  quark PDF at large  $x$ , and in the absence of TMCs ranges from  $\approx 3\%$  at  $x = 0.6$  to  $\approx 11\%$  at  $x = 0.8$  for both  $Q^2 = 2$  and  $10 \text{ GeV}^2$ . This is significantly larger than the TMC uncertainty band in Fig. 12, where the spread of the TMC model predictions is  $\ll 1\%$ , even though the absolute target mass effect is somewhat larger.

The effect of TMCs on the PDF uncertainty, illustrated in Fig. 13 for the OPE prescription, is to reduce the uncertainty band at large  $x$  for the lower  $Q^2$  value, in analogy with the effect seen in Fig. 7 for the  $R_{np}$  ratio, with strength moving from lower  $x$  to higher  $x$  by the  $x \rightarrow \xi$  rescaling of the structure functions. The slightly different effects of TMCs on the various structure functions present in the asymmetry render the uncertainty band on  $A_{\text{PV}}$  more asymmetric at  $Q^2 = 2 \text{ GeV}^2$ . At the higher  $Q^2 = 10 \text{ GeV}^2$  value, the impact of TMCs

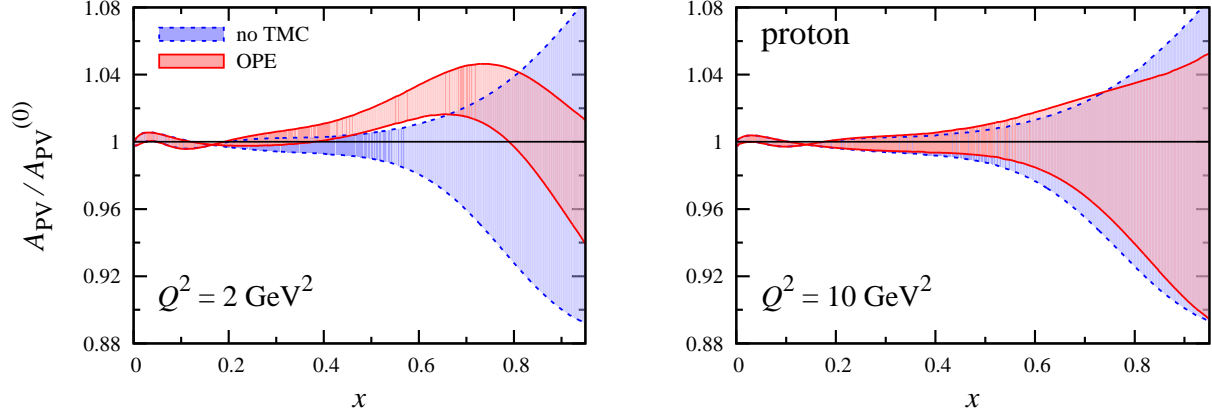


FIG. 13: Proton PVDIS asymmetry  $A_{\text{PV}}$  at  $Q^2 = 2 \text{ GeV}^2$  (**left**) and  $Q^2 = 10 \text{ GeV}^2$  (**right**) for CJ PDFs with minimal and maximal nuclear effects [7] (shaded bands), relative to the asymmetry  $A_{\text{PV}}^{(0)}$  for the central CJ PDF fits, with no TMCs (dashed, blue) and using the OPE TMC prescription (solid, red).

on the uncertainty band is reduced considerably, with the two bands (corresponding to no TMCs and the OPE TMC prescription) approximately coinciding for all  $x$ .

The conclusion from the combined results of Figs. 12 and 13 is that the effect of TMCs and particularly their uncertainties can be minimized in the  $A_{\text{PV}}$  ratio by measuring the asymmetry at values of  $Q^2 \sim 10 \text{ GeV}^2$  or higher; at lower  $Q^2$ , although the TMC uncertainties are not large, some residual corrections will need to be applied in the range  $0.4 \lesssim x \lesssim 0.9$ , where the TMCs are  $\approx 1\%$  or higher.

## 2. Deuteron asymmetry

Unlike for a proton target, for PVDIS on an isoscalar deuterium nucleus most of the dependence on PDFs cancels if one assumes that PDFs in the proton and neutron are related by charge symmetry [25]. In fact, in the valence quark region ( $x \gtrsim 0.5$ ) where sea quarks and gluons can be neglected, the deuteron asymmetry can be written at leading order as [23, 30, 48]

$$A_{\text{PV}}^d \approx - \left( \frac{G_F Q^2}{2\sqrt{2}\pi\alpha} \right) \frac{6}{5} (g_A^e (2g_V^u - g_V^d) + Y_3 g_V^e (2g_A^u - g_A^d)), \quad [x \gg 0], \quad (22)$$

where  $g_V^u = -1/2 + (4/3)\sin^2\theta_W$ ,  $g_V^d = 1/2 - (2/3)\sin^2\theta_W$ ,  $g_A^u = 1/2$ , and  $g_A^d = -1/2$ . (Note that the conventions for  $g_{V,A}^e$  in Ref. [23] differ by a factor 2 compared with those used

here, although the asymmetry is of course independent of the convention.) Consequently accurate measurement of deuteron PVDIS has been proposed as a sensitive test of either the weak mixing angle  $\sin^2 \theta_W$  (deviations of which from its Standard Model value may signal the presence of new physics), or more conventionally of charge symmetry violation (CSV) in PDFs.

Nonzero values of  $\delta u$  and  $\delta d$  are predicted in nonperturbative models of the nucleon to arise from quark mass differences and electromagnetic effects (for a review see Ref. [46]), and can also be generated from radiative QED corrections in  $Q^2$  evolution [49–51]. Defining charge symmetry violating PDFs by

$$\delta u = u^p - d^n, \quad \delta d = d^p - u^n, \quad (23)$$

the PVDIS asymmetry (22) in the presence of CSV is modified according to

$$(2g_{V,A}^u - g_{V,A}^d) \rightarrow (2g_{V,A}^u - g_{V,A}^d)(1 + \Delta_{V,A}), \quad (24)$$

where the fractional CSV corrections are given by

$$\Delta_{V,A} = \left( -\frac{3}{10} + \frac{2g_{V,A}^u + g_{V,A}^d}{2(2g_{V,A}^u - g_{V,A}^d)} \right) \left( \frac{\delta u - \delta d}{u + d} \right). \quad (25)$$

These approximate expressions serve to illustrate explicitly the role of CSV in the PVDIS asymmetry; in practice, however, the full deuteron asymmetry can be computed including the effects of CSV at NLO, as well as sea quarks and gluons.

Using the MRSTQED parametrization of PDFs [50], which generates nonzero values of  $\delta u$  and  $\delta d$  through radiative QED effects, the effect of CSV on the deuteron asymmetry  $A_{\text{PV}}^d$  is illustrated in Fig. 14. In the valence quark region the CSV effect is small at intermediate  $x$ ,  $x \sim 0.4$ , but increases to around 1% at  $x \sim 0.8$ . This is roughly comparable to the earlier fit in Ref. [49] which parametrized the CSV PDFs as  $\delta u - \delta d = 2\kappa\sqrt{x}(1-x)^4(x-0.0909)$ , with  $\kappa = -0.2$  as the best fit parameter. (The constraints on  $\kappa$  were found to be relatively weak, however, and values of  $\kappa$  from  $-0.8$  to  $+0.65$  produced fits at the 90% confidence level, with effects on the asymmetry ranging from  $\approx 4\%$  to  $8\%$  over the range  $0.4 \lesssim x \lesssim 0.8$ .) Deviations of the full NLO result from the valence approximation appear already at  $x \lesssim 0.7$ , however, and these differ quite markedly at small  $x$ , as Fig. 14 indicates. Interestingly, the full asymmetry becomes larger at smaller  $x$  because of CSV effects in the light sea quarks, which produce an asymmetry of about 2% at  $x \approx 0.2$ . On the other

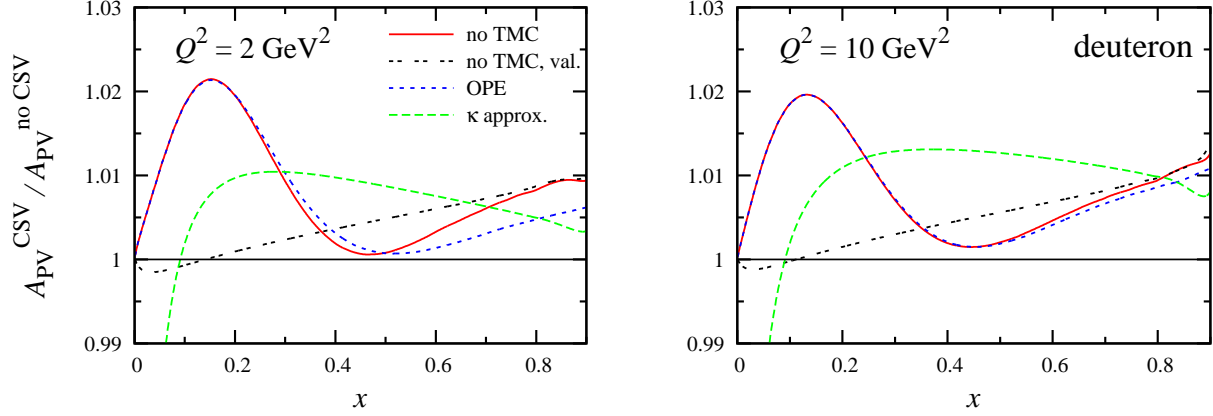


FIG. 14: Deuteron PVDIS asymmetry including CSV effects, relative to the asymmetry with charge-symmetric PDFs, at  $Q^2 = 2 \text{ GeV}^2$  (**left**) and  $Q^2 = 10 \text{ GeV}^2$  (**right**). The CSV PDFs are computed from the MRSTQED parametrization [50] for the full asymmetry (solid, red) and for the valence approximation (double-dashed, black), and from the  $\kappa$ -dependent fit (see text) in Ref. [49] (long-dashed, green). The effects of TMCs on the full asymmetry with the MRSTQED PDFs are illustrated for the OPE prescription (short-dashed, blue).

hand, cleanly separating the CSV effects from sea quark and gluon contributions, which introduce additional  $x$  dependence beyond that in Eqs. (22), (24) and (25), as well as possible differences between CSV in valence and sea quark PDFs, becomes more challenging at small  $x$ .

With sought-after CSV effects that could be  $\lesssim 1 - 2\%$ , it is vital to quantify the impact of TMCs on the deuteron PVDIS asymmetries and in particular the TMC prescription dependence. The effect of TMCs on the full asymmetry relative to the charge-symmetric asymmetry is negligible at  $x \lesssim 0.5$ , but decreases the CSV signal by up to 50% at  $x \approx 0.8$ , as Fig. 14 demonstrates for the OPE prescription. The model dependence of TMCs is illustrated for the various prescriptions in Fig. 15, where the ratio of asymmetries is shown with TMCs to those without TMCs. The net effect is very small, peaking at  $\sim 0.1\%$  at  $x \approx 0.4$ , even at the  $Q^2 = 2 \text{ GeV}^2$  value. The TMC prescription dependence of this ratio is even smaller, making it essentially negligible on the scale of a CSV signal of  $\sim 1\%$ . If the target mass corrected asymmetries were calculated with the charge symmetry violating MRSTQED PDFs, the effect would be somewhat larger, peaking at  $\sim 0.3\%$  around  $x \approx 0.4$ . However, the TMC model dependence is still negligible at around 0.05%. As expected, the impact of TMCs on the deuteron asymmetries at the larger  $Q^2 = 10 \text{ GeV}^2$  value is

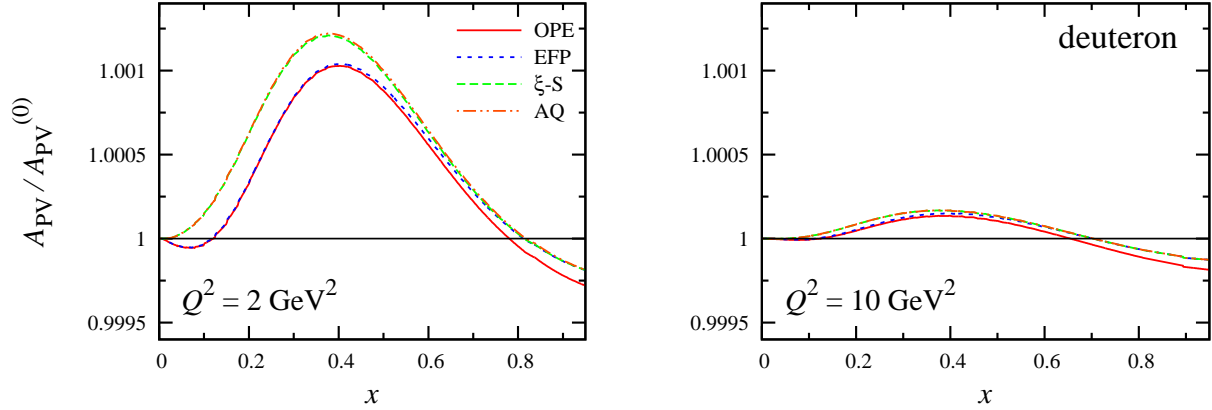


FIG. 15: Ratio of target mass corrected to uncorrected PVDIS deuteron asymmetries  $A_{\text{PV}}^d$  at  $Q^2 = 2 \text{ GeV}^2$  (**left**) and  $Q^2 = 10 \text{ GeV}^2$  (**right**), for the OPE (solid, red), EFP (short-dashed, blue),  $\xi$ -S (long-dashed, green), and AQ (dot-dashed, orange) TMC prescriptions.

considerably smaller. It is therefore likely that TMCs would only play a role in deuteron PVDIS measurements if the CSV effects were on the scale of a fraction of a percent, at which point they would not be discernible within the expected precision of the experiment [13]. The corrections due to nuclear smearing in the deuteron would have similarly negligible effects on the measured deuteron asymmetry.

#### IV. CONCLUSIONS

With the increased precision and kinematic reach of new experiments planned in the next few years, particularly at Jefferson Lab with its 12 GeV upgrade, the need for reliable theoretical tools with which to analyze the data is becoming ever more pertinent. This is especially true for data that will be taken at large values of  $x$ , where a number of different subleading effects come to the fore. In this work we have performed a comprehensive analysis of one class of such corrections, namely those associated with finite values of  $x^2 M^2 / Q^2$ , or target mass corrections. We have detailed several approaches to TMCs, including the standard OPE method, as well as prescriptions based on collinear factorization, and have compared their effects on various spin-averaged structure functions at next-to-leading order.

For the TMCs computed via the OPE, we find that the  $1/Q^2$  and  $1/Q^4$  approximations to the full results are accurate only up to  $x \approx 0.6$ , beyond which the series displays rather slow convergence. Such an expansion has been proposed to avoid the threshold problem at

$x = 1$ ; our findings suggest, however, that a low order expansion may not be applicable as  $x \rightarrow 1$ . Numerically, we find that TMCs in the OPE approach are very similar to those computed via the EFP implementation of collinear factorization, especially for the vector structure functions  $F_1$  (or  $F_L$ ) and  $F_2$ . This can be demonstrated analytically, through the equality to order  $1/Q^2$  of the prefactors associated with the leading terms. The comparative phenomenology of these prescriptions has not previously been addressed in the literature.

Similarly, the  $\xi$ -scaling and AQ prescriptions, which are derived from different approximations within the collinear factorization framework, yield corrected structure functions that closely track each other over much of the  $x$  range accessible experimentally. In all cases the magnitude of the TMCs, and in particular their model dependence is, not surprisingly, significantly more important at low  $Q^2$  values ( $\sim 2 \text{ GeV}^2$ ). Target mass corrections are suppressed with increasing  $Q^2$ , although even at  $Q^2 \sim 10 \text{ GeV}^2$  they are not negligible for some observables at very large  $x$ . The greatest model dependence of TMCs arises for the longitudinal structure function, where because of the mixing between the  $F_L$  and  $F_2$  structure functions the effects for the OPE and EFP prescriptions are significantly larger than for the AQ and  $\xi$ -scaling approaches, where no mixing occurs.

In addition to quantifying the impact of TMCs on structure functions, we further discussed the limitations these place on unambiguously extracting information on PDFs (such as the  $d/u$  ratio or charge symmetry violation) from observables. For the ratio  $R_{np}$  of neutron to proton  $F_2$  structure functions we make the interesting observation that at low  $Q^2$  not only is one subject to greater TMC uncertainties than at large  $Q^2$ , but the  $x \rightarrow \xi$  rescaling due to TMCs effectively also decreases the sensitivity to the  $d/u$  ratio at large  $x$  that measurements of  $R_{np}$  attempt to constrain.

For parity-violating DIS from the proton, the effects of TMCs and perturbative NLO radiative corrections are similar in both the electromagnetic and  $\gamma Z$  interference LT ratios  $R^\gamma$  and  $R^{\gamma Z}$ , with  $\lesssim 4 - 5\%$  differences for  $Q^2 = 2 \text{ GeV}^2$  at intermediate and larger  $x$ . For the deuteron the differences between  $R^\gamma$  and  $R^{\gamma Z}$  are smaller in the valence quark dominated region, with negligible dependence on the TMC prescription, but become larger at very small  $x$  ( $\lesssim 8\%$  and  $4\%$  at  $Q^2 = 2$  and  $10 \text{ GeV}^2$ , respectively) through gluonic contributions at NLO. The magnitude of TMCs in the  $R^{\gamma Z}$  ratio itself, however, is significant at large  $x$ , especially for the OPE and EFP prescriptions. We also considered the effects of nuclear corrections in the deuteron on the  $\gamma Z$  LT ratio, which become important for  $x \gtrsim 0.4 - 0.5$ ;

however, the similarity of these with the effects on the electromagnetic LT ratio leads to nuclear corrections largely canceling in the PVDIS asymmetry.

The effects of TMCs on the parity-violating asymmetries themselves are generally rather small, especially at higher  $Q^2$  values,  $Q^2 \sim 10 \text{ GeV}^2$ , although at lower  $Q^2$  some residual TMC dependence is evident in the case of the proton asymmetry. Measurements of the proton PVDIS asymmetry are planned to provide a unique combination of PDFs in order to constrain the  $d/u$  ratio at large  $x$  [13]. For the deuteron, the size of TMCs is about an order of magnitude smaller than the expected CSV effects in PDFs, which are estimated to be at the  $\mathcal{O}(1\%)$  level. On the other hand, while the corrections to the LT ratios and asymmetries computed here have been perturbative, nonperturbative effects such as those associated with nonzero parton transverse momentum in the nucleon can produce additional strength in the longitudinal structure functions [52]. This may be particularly relevant for the ratio  $R^Z$ , whose phenomenology is essentially unknown at low  $Q^2$ . Estimates of nonperturbative contributions to  $R^Z$  would therefore be necessary before making more definitive conclusions about its role in PVDIS.

In the future, additional effects not discussed here may need to be considered at large  $x$ , principal among which are dynamical higher twist corrections associated with nonperturbative multi-parton correlations. These are very difficult to compute from first principles, and only rudimentary model estimates have been available to date. Further insight into the relation between TMCs and higher twists may also shed light on the threshold problem, whereby the target mass corrected structure functions remain finite at the nucleon elastic scattering point,  $x = 1$ , as well as on the difference between the various TMC prescriptions. Other corrections that may affect future analysis of large- $x$  data are threshold resummations, which involve formally summing, to all orders in  $\alpha_s$ , terms containing logarithms of  $1 - x$  that become large as  $x \rightarrow 1$ . The results on the phenomenology of the target mass corrections contained in the present work should provide a benchmark for future theoretical and experimental investigations of these additional corrections. This analysis can also be extended to the spin-dependent sector [53–56], where the phenomenology of the collinear factorization framework in particular has not been as fully developed.

## Acknowledgements

This work was supported by the DOE contract No. DE-AC05-06OR23177, under which Jefferson Science Associates, LLC operates Jefferson Lab, DoD's ASSURE Program, and the National Science Foundation under NSF Contact Nos. 1062320 and 1002644.

---

- [1] A. D. Martin, W. J. Stirling, R. S. Thorne and G. Watt, *Eur. Phys. J. C* **63**, 189 (2009).
- [2] P. Jimenez-Delgado and E. Reya, *Phys. Rev. D* **79**, 074023 (2009).
- [3] S. Alekhin, J. Blümlein, S. Klein and S. Moch, *Phys. Rev. D* **81**, 014032 (2010).
- [4] F. D. Aaron *et al.*, *JHEP* **1001**, 109 (2010).
- [5] H. -L. Lai *et al.*, *Phys. Rev. D* **82**, 074024 (2010).
- [6] A. Accardi *et al.*, *Phys. Rev. D* **81**, 034016 (2010).
- [7] A. Accardi *et al.*, *Phys. Rev. D* **84**, 014008 (2011).
- [8] R. D. Ball *et al.*, *Nucl. Phys.* **B855**, 153 (2012).
- [9] L. W. Whitlow *et al.*, *Phys. Lett. B* **282**, 475 (1992).
- [10] M. E. Christy and W. Melnitchouk, *J. Phys. Conf. Ser.* **299**, 012004 (2011).
- [11] Jefferson Lab Experiment E12-10-102 [BONUS12], S. Bültmann, M. E. Christy, H. Fenker, K. Griffioen, C. E. Keppel, S. Kuhn and W. Melnitchouk, spokespersons.
- [12] Jefferson Lab Experiment E12-10-103 [MARATHON], G. G. Petratos, J. Gomez, R. J. Holt and R. D. Ransome, spokespersons.
- [13] Jefferson Lab Experiment E12-10-007 [SoLID], P. Souder, spokesperson.
- [14] L. T. Brady, A. Accardi, W. Melnitchouk and J. F. Owens, arXiv:1110.5398 [hep-ph].
- [15] S. Kuhlmann *et al.*, *Phys. Lett. B* **476**, 291 (2000).
- [16] O. Nachtmann, *Nucl. Phys. B* **63**, 237 (1973).
- [17] H. Georgi and H. D. Politzer, *Phys. Rev. D* **14**, 1829 (1976).
- [18] I. Schienbein *et al.*, *J. Phys. G* **35**, 053101 (2008).
- [19] R. K. Ellis, W. Furmanski and R. Petronzio, *Nucl. Phys. B* **212**, 29 (1983).
- [20] M. A. G. Aivazis, F. I. Olness and W. K. Tung, *Phys. Rev. D* **50**, 3085 (1994).
- [21] S. Kretzer and M. H. Reno, *Phys. Rev. D* **66**, 113007 (2002).
- [22] A. Accardi and J. W. Qiu, *JHEP* **07**, 090 (2008).

- [23] T. Hobbs and W. Melnitchouk, Phys. Rev. D **77**, 114023 (2008). Note that in Eqs. (9) and (13) the mass-dependent correction factor should have the energy  $E$  replaced by  $2E$ .
- [24] T. Hobbs, AIP Conf. Proc. **1369**, 51 (2011).
- [25] J. D. Bjorken, Phys. Rev. D **18**, 3239 (1978).
- [26] S. Fajfer and R. J. Oakes, Phys. Rev. D **30**, 1585 (1984).
- [27] P. Castorina and P. J. Mulders, Phys. Rev. D **31**, 2760 (1985).
- [28] S. Mantry, M. J. Ramsey-Musolf and G. F. Sacco, Phys. Rev. C **82**, 065205 (2010).
- [29] A. V. Belitsky, A. Manashov and A. Schäfer, Phys. Rev. D **84**, 014010 (2011).
- [30] K. Nakamura *et al.*, J. Phys. G **37**, 075021 (2010).
- [31] O. W. Greenberg and D. Bhaumik, Phys. Rev. D **4**, 2048 (1971).
- [32] K. Bitar, P. W. Johnson and W. K. Tung, Phys. Lett. B **83** (1979) 114; P. W. Johnson and W. K. Tung, Print-79-1018 (Illinois Tech), Contribution to Neutrino '79, Bergen, Norway (1979).
- [33] F. M. Steffens and W. Melnitchouk. Phys. Rev. C **73**, 055202 (2006).
- [34] S. A. Kulagin and R. Petti, Nucl. Phys. A **765** (2006) 126.
- [35] A. Accardi, T. Hobbs and W. Melnitchouk, JHEP **11**, 084 (2009).
- [36] J. -W. Qiu, Phys. Rev. **D42**, 30-44 (1990).
- [37] G. Altarelli and G. Martinelli, Phys. Lett. B **76**, 89 (1978).
- [38] W. A. Bardeen, A. J. Buras, D. W. Duke and T. Muta, Phys. Rev. D **18**, 3998 (1978).
- [39] J. C. Collins, D. E. Soper and G. F. Sterman, Adv. Ser. Direct. High Energy Phys. **5**, 1 (1988).
- [40] W. Melnitchouk and A. W. Thomas, Phys. Lett. B **377**, 11 (1996).
- [41] I. R. Afnan *et al.*, Phys. Lett. B **493**, 36 (2000); Phys. Rev. C **68**, 035201 (2003).
- [42] W. Melnitchouk, R. Ent and C. E. Keppel, Phys. Rep. **406**, 127 (2005).
- [43] Y. Kahn, W. Melnitchouk and S. A. Kulagin, Phys. Rev. C **79**, 035205 (2009).
- [44] J. J. Aubert *et al.*, Phys. Lett. B **123**, 275 (1983); D. F. Geesaman, K. Saito and A. W. Thomas, Ann. Rev. Nucl. Part. Sci. **45**, 337 (1995).
- [45] P. A. Souder, AIP Conf. Proc. 747, 199 (2005).
- [46] J. T. Londergan and A. W. Thomas, J. Phys. G **31**, 1151 (2005).
- [47] C. Y. Prescott *et al.*, Phys. Lett. **77 B**, 347 (1978); C. Y. Prescott *et al.*, Phys. Lett. **84 B**, 524 (1979); R. N. Cahn and F. J. Gilman, Phys. Rev. D **17**, 1313 (1978).
- [48] M. Anselmino, P. Gambino and J. Kalinowski, Z. Phys. C **64**, 267 (1994).

- [49] A. D. Martin, R. G. Roberts, W. J. Stirling and R. S. Thorne, Eur. Phys. J. C **35**, 325 (2004).
- [50] A. D. Martin, R. G. Roberts, W. J. Stirling and R. S. Thorne, Eur. Phys. J. C **39**, 155 (2005).
- [51] M. Gluck, P. Jimenez-Delgado and E. Reya, Phys. Rev. Lett. **95**, 022002 (2005);  
arXiv:hep-ph/0501169.
- [52] R. P. Feynman, *Photon-Hadron Interactions*, Benjamin, Reading, MA (1972).
- [53] J. Blümlein and A. Tkabladze, Nucl. Phys. **B553**, 427 (1999).
- [54] W. Detmold, Phys. Lett. B **632**, 261 (2006).
- [55] A. Accardi and W. Melnitchouk, Phys. Lett. B **670**, 114 (2008).
- [56] U. D'Alesio, E. Leader and F. Murgia, Phys. Rev. D **81**, 036010 (2010).